Journal of Materials Chemistry A

ROYAL SOCIETY OF CHEMISTRY

PAPER

View Article Online
View Journal | View Issue

Cite this: J. Mater. Chem. A, 2020, 8, 24608

Triple-cation low-bandgap perovskite thin-films for high-efficiency four-terminal all-perovskite tandem solar cells†

Somayeh Moghadamzadeh, *[ab] Ihteaz M. Hossain,[ab] The Duong, [c] Saba Gharibzadeh,[ab] Tobias Abzieher,[ab] Huyen Pham,[d] Hang Hu,[ab] Paul Fassl, [ab] Uli Lemmer,[ab] Bahram Abdollahi Nejand *[ab] and Ulrich W. Paetzold *[ab]

All-perovskite multi-junction photovoltaics, comprised of a wide-bandgap (WBG) and a low-bandgap (LBG) perovskite solar cell (PSC), has opened a new window to cost-effective yet highly efficient solar cells (>33%). However, the poor operational stability of LBG PSCs is a major obstacle to the technological advance of all-perovskite tandem solar cells (all-PTSC). This study demonstrates that introducing minute quantities of Cs (1–10%) into the LBG $FA_{0.8}MA_{0.2}Sn_{0.5}Pb_{0.5}I_3$ perovskite semiconductors ($E_g = 1.26$ eV) significantly improves the operational photo-stability of the corresponding LBG PSCs, due to a reduction of residual nanosized $Sn_yPb_{(1-y)}I_2$ aggregates, resulting in a beneficial stoichiometric composition. For an optimal concentration of Cs (2.5%) in the investigated range, the LBG PSCs attain remarkable power conversion efficiency (PCE) as high as 18.2% and maintain up to 92% of their initial power output after two hours under simulated one sun illumination. By mechanically stacking high-performance LBG bottom PSCs with semi-transparent top PSCs (E_g = 1.65 eV), four-terminal all-PTSCs with high PCE of 23.6% are attainable.

Received 31st July 2020
Accepted 23rd October 2020

DOI: 10.1039/d0ta07005j

rsc.li/materials-a

1. Introduction

The rapid growth in power conversion efficiency (PCE) of single-junction organic–inorganic perovskite solar cells (PSCs) from 3.8% to 25.5% over the past few years[1,2] has attracted intensive attention and encouraged further investigations in the perovskite field. While the PCE of single-junction PSCs is limited to the theoretical Shockley–Queisser (SQ) radiative efficiency (31–33%),[3] tandem technologies offer a route to surpass the SQ limit by combining a top solar cell with a wide-bandgap (WBG) absorber and a bottom solar cell with a low-bandgap (LBG) absorber, through either two-terminal (2T) or four-terminal (4T) tandem configurations. Metal halide perovskite semiconductors (with a chemical structure of ABX_3) composed of a variety of chemical components comprised of organic and/or inorganic cations (A = formamidinium (FA^+); methylammonium (MA^+); cesium (Cs^+)), divalent metals (B = lead (Pb^{2+}); tin (Sn^{2+}); germanium (Ge^{2+})), and halide anions (X = iodide (I^-); bromide (Br^-); chloride (Cl^-)), possess a wide range of bandgaps between 1.10–1.55 eV (ref. 4 and 5) and 1.5–2.3 eV (ref. 6–8) by tuning the Sn : Pb and I : Br ratio, respectively. Therefore, this class of materials is suited for both WBG top and LBG bottom solar cells in an all-perovskite tandem solar cell (all-PTSC) configuration.[9–16] All-PTSCs with current record PCEs of 25.4% for a 4T[17] and 24.8% for a 2T[18] configuration benefit from simple and potentially cost-effective fabrication processes *via* both solution[19] and vapor[20,21] deposition methods. However, to date, the low operational stability and performance of LBG bottom PSCs is one of the major hurdles towards high-efficiency all-PTSCs. Therefore, investigating strategies that address the poor stability of LBG PSCs is essential.

Partial substitution of Sn^{2+} for Pb^{2+} in pure Pb-based perovskite semiconductors desirably lowers the bandgap to 1.1–1.3 eV, which is suited for LBG bottom solar cells in all-PTSCs.[4,13,22–24] Unlike Pb, Sn is prone to oxidation from Sn^{2+} to Sn^{4+}. Therefore the Sn–Pb-based PSCs suffer from lower stability even in an inert atmosphere with a trace amount of oxygen.[18,25,26] The most common strategies to prevent oxidation are incorporating antioxidant additives such as SnF_2,[26–30] $SnBr_2$,[26,27,31] $SnCl_2$,[27,32] GuaSCN,[17] ascorbic acid,[33] and sulfonic acid group,[34] applying 2D components as passivation layers,[35–37] compositional engineering,[38] as well as utilizing Sn-reduced precursor solutions.[18,39] In addition to the oxygen-induced degradation, other possible degradation mechanisms such as

[a]Light Technology Institute, Karlsruhe Institute of Technology, Engesserstrasse 13, 76131 Karlsruhe, Germany. E-mail: somayeh.moghadamzadeh@kit.edu
[b]Institute of Microstructure Technology, Karlsruhe Institute of Technology, Hermann-von-Helmholtz-Platz 1, 76344 Eggenstein-Leopoldshafen, Germany
[c]Research School of Electrical, Energy and Materials Engineering, The Australian National University, Canberra 2601, Australia
[d]Department of Electronic Materials Engineering, Research School of Physics, The Australian National University, Canberra 2601, Australia

† Electronic supplementary information (ESI) available. See DOI: 10.1039/d0ta07005j

thermal decomposition,[40,41] light-induced degradation,[41,42] and crystal-structure transition[43,44] are less explored for Sn–Pb-based PSCs. The crystal structure of perovskite semiconductors strongly affects the thermal and phase-stability of perovskite thin-films. In that regard, compositional engineering is an established strategy to adapt the crystal-structure of ABX_3, which is determined by the size and interaction of the A-site and the BX_6 octahedra.[45] To form a stable perovskite structure, the Goldschmidt tolerance factor, $t = \frac{r_A + r_X}{\sqrt{2}(r_B + r_X)}$, where r_A, r_B, and r_X are the radii of the respective atoms, is supposed to be between 0.8 and 1.0.[45] Implementing mixed cations at the A-site is a well-established approach to tune t in the relevant range. For example, incorporating small quantities of Cs into the crystalline lattice of double-cation $FA_xMA_{(1-x)}$ perovskite semiconductors is reported to improve structural stability and the optoelectronic properties of Pb-based perovskite absorber layers.[46,47] As reported, the lattice alterations result in a reduction in trap density in the bulk and the grain boundaries, thereby reducing non-radiative recombination rate and improving the performance and the stability of corresponding PSCs.[46,47] Similarly, incorporating Cs in Sn–Pb-based perovskite is reported to have beneficial effects on the photovoltaic performance of LBG PSCs.[13,14,38,48] Leijtens *et al.* demonstrated that a total substitution of Cs for MA in an $FA_{0.6}MA_{0.4}Sn_{0.6}Pb_{0.4}I_3$ composition leads to an enhanced thermal and operational stability in the respective PSCs.[14] Furthermore, it was verified that Cs incorporation into mono-cation Sn–Pb-based perovskite reduces the crystallization rate, leading to an improved film formation, which effectively suppresses the Sn^{2+} oxidation if exposed to the ambient environment.[38] The open-circuit voltage (V_{OC}) and the short-circuit current (J_{SC}) of $MASn_{0.5}Pb_{0.5}I_3$ and $FASn_{0.5}Pb_{0.5}I_3$ LBG PSCs are reported to be considerably improved by incorporating Cs into the crystal structure.[38] A recent study investigated the role of Cs when integrated into a double-cation $FA_{0.5}MA_{0.5}Sn_{0.5}Pb_{0.5}I_3$ LBG perovskite.[48] According to the results, a strain reduction induced by the addition of Cs results in reduced trap densities, and therefore improves the optoelectronic performance of the corresponding PSCs.[48] Aside from the above-mentioned studies, in which the incorporation of Cs was shown to effectively improve the efficiency of LBG PSCs, the possible effects of Cs incorporation in improving the photo-stability of Sn–Pb-based LBG PSCs have not been investigated yet.

In this work, we study LBG PSCs with the absorber composition $Cs_x(FA_{0.8}MA_{0.2})_{(1-x)}Sn_{0.5}Pb_{0.5}I_3$ (with $x = 0\%$, 1%, 2.5%, 5%, and 10%) and demonstrate significantly improved photo-stability upon introducing minute amounts of Cs with PCEs as high as 18.2% for $x = 2.5\%$. Our analyses, based on scanning electron microscopy (SEM), cathodoluminescence (CL), and X-ray diffraction (XRD) reveal that Cs incorporation mitigates the formation of nanosized $Sn_yPb_{(1-y)}I_2$ aggregates (with $0 < y < 1$) at the interface of the perovskite absorber and the electron transport layer (ETL). This mitigation correlates to the photovoltaic performance of the PSC devices, such that for a specific Cs concentration in the investigated range PSCs attain enhanced operational photo-stability. Finally, combining the highest-performing triple-cation LBG PSCs ($E_g = 1.26$ eV) with semi-transparent double-cation PSCs ($E_g = 1.65$ eV), we report on 4T all-PTSCs with PCE as high as 23.6%.

2. Results and discussion

Given the rapid crystallization rate, the formation of high-quality solution-processed Sn-based perovskite thin-films is more challenging to control compared to their Pb-based counterparts.[15] In a previous publication, we introduced the vacuum-assisted growth control (VAGC) method as an efficient strategy to process pin-hole free Sn-based perovskite thin-films.[16] Applying the same method here, we prepare mixed Sn–Pb perovskite thin-films in the composition $Cs_x(FA_{0.8}MA_{0.2})_{(1-x)}Sn_{0.5}Pb_{0.5}I_3$ with $x = 0\%$, 1%, 2.5%, 5%, and 10%, hereafter denoted as Cs0%, Cs1%, Cs2.5%, Cs5% and Cs10%, respectively. The experimental section provides the reader with more details on the PSC devices and perovskite thin-films fabrication. Fig. 1a illustrates the layer sequence of a LBG PSC consisting of glass/indium tin oxide (ITO) (230 nm)/poly[bis(4-phenyl)(2,4,6-trimethylphenyl)amine] (PTAA) (6 nm)/$Cs_x(FA_{0.8}MA_{0.2})_{(1-x)}Sn_{0.5}Pb_{0.5}I_3$ (~550 nm)/phenyl-C_{61}-butyric acid methyl ester (PCBM) (8 nm)/buckminsterfullerene (C_{60}) (25 nm)/2,9-dimethyl-4,7-diphenyl-1,10-phenanthroline (BCP) (3 nm)/silver (Ag) (100 nm), together with a cross-sectional SEM image of the same layer stack with a Cs2.5% perovskite thin-film. Fig. S1a† depicts a cross-sectional SEM image of a PSC with the same layer stack with Cs0% perovskite thin-film. In Fig. 1b, we compare maximum power point (MPP) tracking results of LBG PSCs prepared with different Cs concentrations that are measured for 120 min under constant air-mass 1.5 global (AM 1.5G) solar illumination at 25 °C in a N_2-filled glovebox (O_2 < 0.2 ppm; H_2O < 0.4 ppm). Notably, incorporating Cs in very small quantities enhances the operational photo-stability of LBG PSCs, such that the stabilized PCE (SPCE) of the PSCs with Cs2.5% and Cs5% maintain 92% and 99% of their initial values after 120 min of MPP tracking, respectively. Compared to the PSC with Cs0%, for which the PCE degrades to 61% of its initial value, the beneficial role of Cs in improving the photo-stability of the PSC devices is apparent. The absolute values of the PCE for the PSCs with different Cs concentrations over 5 and 120 min are shown in the inset of Fig. 1b and S1b,† respectively. A champion PSC with an optimized Cs concentration of 2.5% exhibits an initial SPCE of 17.5%. It should be noted that this level of stability for Sn–Pb-based perovskite has been attained in the absence of additives such as GuaSCN[17] or incorporation of Br^- and Cl^-.[49,50] Fig. S1c† compares the current-density–voltage (J–V) scans of the champion PSCs prepared with different Cs concentrations, among which PSC with Cs2.5% exhibits the highest PCE of 18.2% in the backward scan direction, enabled by J_{SC} over 32 mA cm^{-2}, which is among the highest currently reported. The integrated J_{SC} values calculated from the external quantum efficiency (EQE) responses of the PSCs with Cs0%, Cs1%, Cs2.5%, Cs5%, and Cs10% (Fig. S1d†) are 29.4, 29.5, 31.4, 29.0, 27.3 mA cm^{-2}, respectively, which confirm the trend observed in the J–V scans. To indicate the reproducibility of the results, we repeat the MPP tracking measurement for six PSCs of

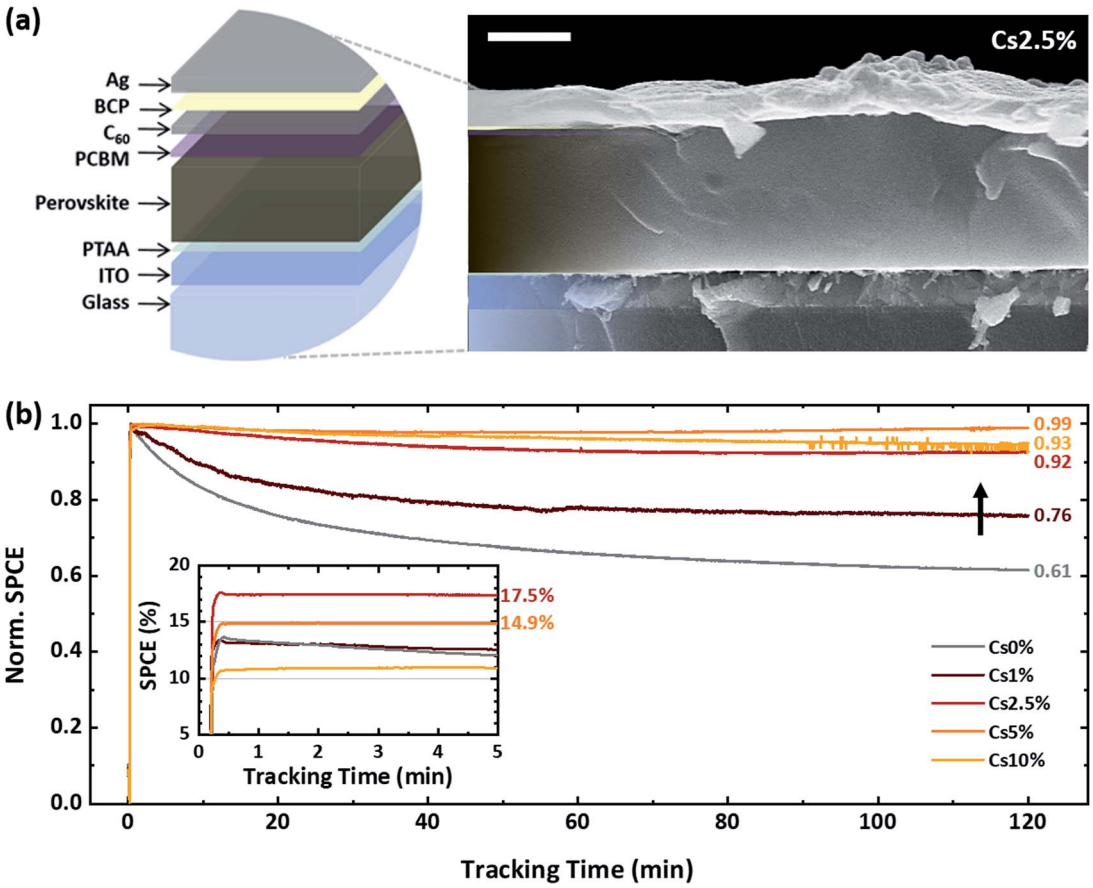

Fig. 1 (a) Schematic illustration and a cross-sectional scanning electron microscopy (SEM) image of a low-bandgap (LBG) perovskite solar cell (PSC) composed of a triple-cation $Cs_x(FA_{0.8}MA_{0.2})_{(1-x)}Sn_{0.5}Pb_{0.5}I_3$ LBG perovskite absorber layer with $x = 2.5\%$ (denoted as Cs2.5%). The scalebar on the top-left is indicative of 300 nm. (b) Stabilized power conversion efficiency (SPCE) of the best performing $Cs_x(FA_{0.8}MA_{0.2})_{(1-x)}Sn_{0.5}Pb_{0.5}I_3$ LBG PSCs with different Cs concentrations varying from $x = 0\%$, to 1%, 2.5%, 5%, and 10% (denoted as Cs0%, Cs1%, Cs2.5%, Cs5%, and Cs10%, respectively) under AM 1.5G illumination (100 mW cm^{-2}) at MPP tracking conditions at 25 °C for 120 min; SPCE are normalized to their initial values (when the light is switched on). Inset: absolute values of the initial SPCE for the same PSCs over the first 5 min.

each Cs concentration that are identically prepared in different batches. Fig. S2,† exhibits the results of the MPP tracking of these devices at 0 min (when the light is switched on) and after 5 and 120 min, which is following the same trend as Fig. 1b. Furthermore, based on the *J–V* characteristics derived from 30 LBG PSCs of each Cs concentration, which were identically prepared in 10 different batches, the average PCE of the PSCs with Cs2.5% is the highest in the investigated range (0% to 10%) (Fig. S3 and Table S1†). We observe that the performance of the PSCs enhances slightly after one night being stored in an N_2-filled glovebox with an oxygen level less than 0.2 ppm in the dark, which is due to a slight improvement mainly in V_{OC} and fill factor (FF) (Fig. S4†). We relate this enhancement to the spontaneous enhancement phenomenon that has been previously reported for PSCs with various perovskite compositions and structures.[51–54] As portrayed in our previous work,[55] spontaneous enhancement in the PCE of PSCs is a general phenomenon and possibly occurs due to a reduction in strain-induced trap states in the bulk of the perovskite materials, which happens gradually over time due to strain relaxation.

To understand the role of Cs in the photovoltaic enhancement of the PSCs, we study the morphology and photo-physics of the perovskite thin-films in the following. SEM images (Fig. 2a) reveal that the perovskite thin-films with Cs0% to Cs5% are all compact and pinhole-free. In contrast, perovskite thin-films with Cs10% exhibit pinholes and cracks between the grains denoting a poor morphology with inhomogeneous coverage, which results in reduced photovoltaic performance in the respective PSCs (Fig. S3†). We also note that the size of the perovskite grains enlarges by increasing Cs concentration (from 217 nm for Cs0% to 570 nm for Cs10%), which is indicative of fewer grain boundaries, and therefore limited non-radiative recombination due to fewer trap states at the grain boundaries.[56] Grain boundaries might result in increased recombination losses and decreased device stability under illumination due to defect-induced ion migration.[57–59] Furthermore, SEM images exhibit the formation of bright nanosized aggregates (<100 nm) on the surface of LBG perovskite thin-films. These aggregates are mitigated by adding Cs and completely disappear by increasing the Cs concentration to 10% (Fig. 2a). The

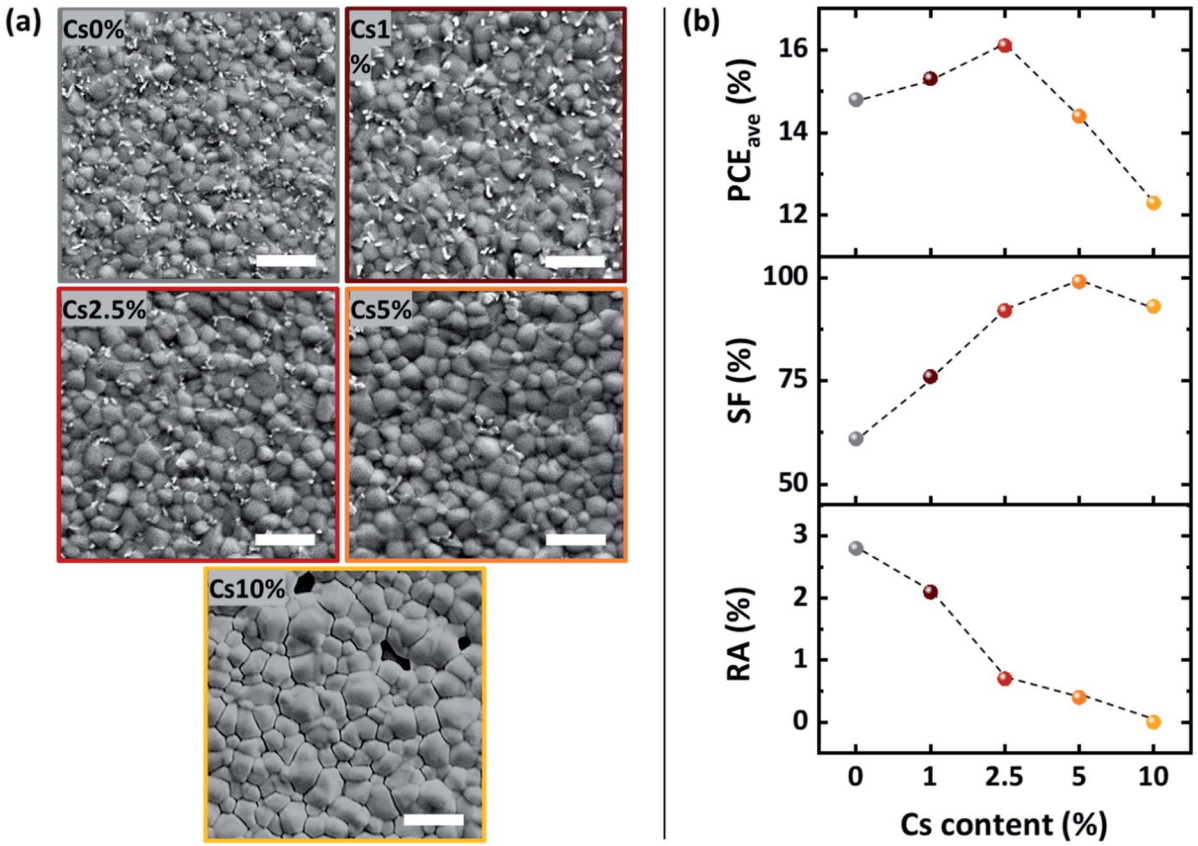

Fig. 2 (a) Top-view scanning electron microscopy (SEM) images of $Cs_x(FA_{0.8}MA_{0.2})_{(1-x)}Sn_{0.5}Pb_{0.5}I_3$ low-bandgap perovskite thin-films with Cs concentrations varying from $x = 0\%$, to 1%, 2.5%, 5%, and 10% (denoted as Cs0%, Cs1%, Cs2.5%, Cs5%, and Cs10%, respectively) deposited by the vacuum-assisted growth control method. The scalebar is indicative of 1 μm. (b) Comparison of the relative area (RA) of the bright nanosized aggregates (=area of the aggregates/area of the grains), the stability factor ($SF = SPCE_{final}/SPCE_{initial}$), and the average PCE ($PCE_{ave}$) of the PSC devices, as a function of Cs content. $SPCE_{final}$ and $SPCE_{initial}$ are the initial (when the light is switched on) and final (after 120 min) values of the SPCE derived from maximum power point (MPP) tracking under constant AM 1.5G solar illumination at 25 °C.

approximate relative area (RA) of the bright nanosized aggregates is compared with the stability factor (SF) and the average PCE (PCE_{ave}) of the PSCs as a function of Cs concentration in Fig. 2b. For the investigated range, there seems to be an optimal amount of Cs (2.5%) to obtain the highest PCEs, while a higher Cs concentration (5%) is beneficial for device photo-stability. Residual PbI_2 is reported to cause degradation of the established Pb-based perovskite thin-films under illumination even in an inert atmosphere.[60–63] Therefore, having verified that incorporating Cs decreases the aggregates observed on the surface of LBG perovskite thin-films and improves the operational photo-stability of the respective PSCs (Fig. 2b), one may hypothesize that these nanosized aggregates are residual PbI_2 crystals that suffer from an intrinsic photo-instability caused by photo-decomposition under illumination.[60,61,64,65] However, considering the chemical structure of our LBG perovskite, containing Sn and Pb, the bright nanosized aggregates might be also composed of residual SnI_2 or $Sn_yPb_{(1-y)}I_2$. CL is a suitable characterization technique to detect phase segregations and residual materials such as PbI_2 excess in perovskite thin-films.[66–69] We compare CL spectra of LBG perovskite thin-films with different Cs concentrations within the spectral range from 400 to 900 nm (Fig. 3a). A broad CL peak located at around 600 nm gradually diminishes with increasing the concentration of Cs from 0% to 10%. This peak indicates the presence of a WBG phase or a material with a bandgap of about 2.1 eV, which is much higher than the bulk bandgap of LBG perovskite thin-films (~1.26 eV). For comparison, we show CL spectra of pure PbI_2, pure SnI_2, mixed $Sn_{0.5}Pb_{0.5}I_2$ thin-films. As presented in Fig. 3b, PbI_2 and SnI_2 thin-films exhibit narrow CL peaks at 505 and 518 nm, respectively. In contrast, the $Sn_{0.5}Pb_{0.5}I_2$ thin-film exhibits a broad CL peak located at around 618 nm, which matches well with the CL emission peak around 600 nm determined for LBG perovskite thin-films. It should be noted that the trend observed for the bandgap of $Sn_yPb_{(1-y)}I_2$ (for $y = 0$, 0.5, and 1), which does not comply with Vegard's law, is similar to the trend reported for the bandgap of $MASn_xPb_{(1-x)}I_3$ thin-films[4] and is attributed to the "band inversion" in the literature.[70,71] In conclusion, the CL suggest that the nanosized aggregates identified in the SEM images are mixed $Sn_yPb_{(1-y)}I_2$ composites with $0 < y < 1$, the amount of which decreases with increasing the amount of Cs.

To provide more insights into the role of Cs in decreasing the amount of these nanosized aggregates, as well as its effect on

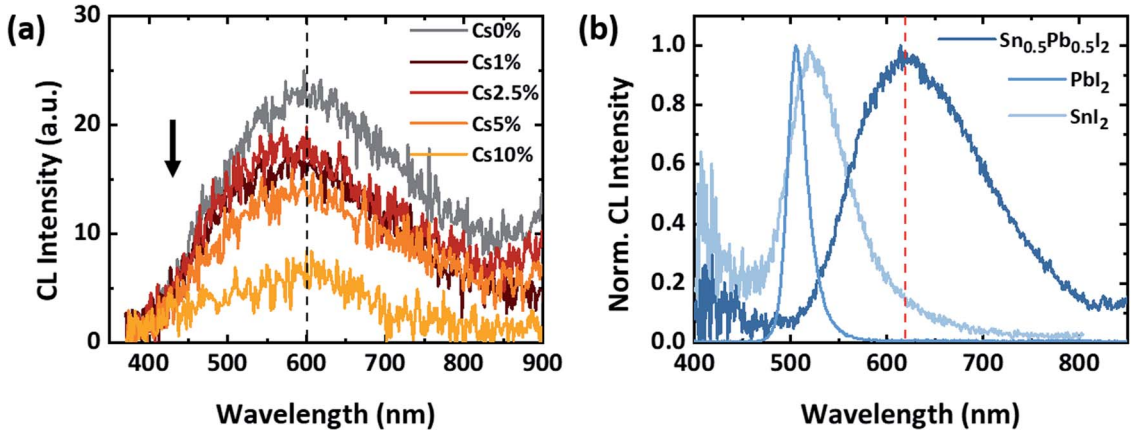

Fig. 3 Cathodoluminescence (CL) spectra of a (a) $Cs_x(FA_{0.8}MA_{0.2})_{(1-x)}Sn_{0.5}Pb_{0.5}I_3$ low-bandgap perovskite thin-films prepared by different Cs concentrations varying from $x = 0\%$, to 1%, 2.5%, 5%, and 10% (denoted as Cs0%, Cs1%, Cs2.5%, Cs5%, and Cs10%, respectively), and (b) PbI_2, SnI_2, and $Sn_{0.5}Pb_{0.5}I_2$ thin-films.

the crystallinity of LBG perovskite thin-films, we perform XRD measurements on perovskite thin-films with different Cs concentrations. The characteristic XRD peak of the underlying ITO substrate thin-film serves as a reference to precisely calibrate the XRD diffraction patterns. The XRD pattern of the perovskite thin-films with and without Cs exhibit two dominant perovskite peaks at 14.1° and 28.3° (Fig. 4a), which are assigned to the (002)/(110) and (004)/(220) planes of the tetragonal perovskite crystal-structure, respectively.[12] We note that by increasing the Cs concentration from 0% to 5%, the intensity of these two characteristic peaks gradually increases, denoting a gradual change in the crystal orientation and/or the crystallinity of the perovskite thin-films. By contrast, perovskite thin-film with Cs10% exhibits the lowest XRD perovskite peak intensities, possibly caused by approaching the substitution limit (spinodal decomposition)[46,72,73] and/or too high excess of cations in the perovskite precursor solution.[63,64] Therefore, according to the XRD and SEM findings, incorporating Cs up to 5% leads to an enhanced crystallinity and/or preferential crystal orientation that correlates well with the gradual increase in the grains' sizes and the enhanced photovoltaic performance of the devices. We also notice a slight shift of the perovskite peaks to higher diffraction angles by increasing the concentration of Cs from 0% to 10% (Fig. S5a†).This shift indicates that Cs is incorporated into the perovskite lattice resulting in a lattice contraction since the ionic radius of Cs^+ (1.81 Å) is much smaller than FA^+ (2.79 Å) and MA^+ (2.70 Å).[38,46] The incorporation of Cs into the perovskite lattice is also confirmed by X-ray photo electron spectroscopy (XPS) presented in Fig. S5b.† The incorporation of Cs into the Sn–Pb-based perovskite material is reported to reduce the crystallization rate and effectively slows down the oxidation of Sn^{2+} to Sn^{4+}, possibly as a result of lattice contraction and denser morphology of the perovskite thin-films.[38] Most importantly, the XRD data manifest that as the concentration of Cs increases, the intensity of the small peak detected at 12.77° abates until it completely disappears for Cs10% (Fig. 4a, inset). XRD results derived from pure PbI_2, pure SnI_2, and $Sn_{0.5}Pb_{0.5}I_2$ thin-films exhibit peaks at 12.65°, 12.76°, and 12.67°, respectively (Fig. S6†). While the signal quality of the XRD data of the perovskite thin-films (Fig. 4a) does not easily allow us to discriminate between these materials, by

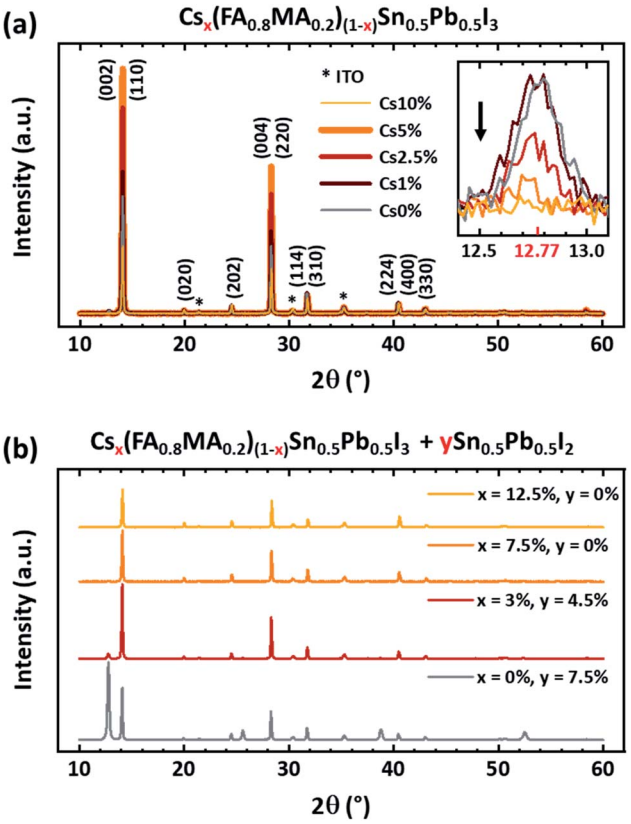

Fig. 4 X-ray diffraction (XRD) patterns of (a) $Cs_x(FA_{0.8}MA_{0.2})_{(1-x)}Sn_{0.5}Pb_{0.5}I_3$ low-bandgap perovskite thin-films with different Cs concentrations varying from $x = 0\%$, to 1%, 2.5%, 5%, and 10% (denoted as Cs0%, Cs1%, Cs2.5%, Cs5%, and Cs10%, respectively); inset exhibits suppression of the XRD peak at 12.77° by increasing Cs content. (b) $Cs_x(FA_{0.8}MA_{0.2})_{(1-x)}Sn_{0.5}Pb_{0.5}I_3$ prepared with a varying excess of Sn and Pb ($ySn_{0.5}Pb_{0.5}I_2$) from $y = 7.5\%$, to 4.5% and 0% depending on the Cs concentrations which varies from $x = 0\%$, to 3%, 7.5%, and 12.5%.

considering both XRD and CL results, we assign this peak to mixed $Sn_yPb_{(1-y)}I_2$ ($0 < y < 1$) that shrinks gradually upon adding more Cs, in line with the decreased amount of nanosized aggregates as observed with SEM. Given that these aggregates are located on the surface of LBG perovskite thin-films and have a bandgap of about 2.1 eV (as detected by CL), they could potentially mitigate the extraction of electrons from the perovskite thin-film to the PCBM ETL, and therefore reduce the operational photo-stability of the PSCs under constant illumination, as previously shown in Fig. 1b.

To shed more light on the effectiveness of Cs in the diminution of residual $Sn_yPb_{(1-y)}I_2$, we carry out further XRD analyses on $Cs_x(FA_{0.8}MA_{0.2})_{(1-x)}Sn_{0.5}Pb_{0.5}I_3$ thin-films that we intentionally prepared with prominent 7.5% of Sn and Pb excess, and varied the Cs concentration from $x = 0\%$ to 3%, 7.5%, and 12.5% (Fig. 4b). In the absence of Cs, there is a dominant peak at around 12.77° (in agreement with the small XRD peak detected for the LBG perovskite thin-films prepared without excess Sn and Pb (Fig. S4a†)) that is ascribed to the existence of large amount of residual $Sn_yPb_{(1-y)}I_2$. This peak significantly abates by adding only a minute amount of Cs ($x = 3\%$), whereas the two main perovskite peaks detected at 14.1° and 28.3° are strongly intensified. Further increasing the amount of Cs results in further decrease ($x = 7.5\%$) and complete disappearance ($x = 12.5\%$) of the $Sn_yPb_{(1-y)}I_2$ XRD peak, with the perovskite peaks starting to exhibit a decrease at the same time. Ultraviolet-visible (UV-vis) spectroscopy of the samples (Fig. S7a†) exhibit that the absorption of the thin-films with $x = 3\%$ and 7.5% increases, whereas it significantly drops for $x = 12.5\%$, in line with the average thickness of the thin-films, which are 490, 516, 534, and 300 nm for $x = 0\%$, 3.5%, 7.5% and 12.5%, respectively (Fig. S7c†). The reduced absorption and layer thickness for a too large Cs concentration might be related to a substitution limit (spinodal decomposition)[46,72,73] and/or too high excess of cations in the precursor solution,[63,64] as discussed above. Since the bandgap of the thin-films with $x = 3\%$ and 7.5% is not altered by the amount of Cs content as evidenced in Fig. S7b,† an increase in their absorption can be indicative of a volumetric growth of the perovskite material, which agrees with the enhanced perovskite XRD peaks (Fig. 4b).

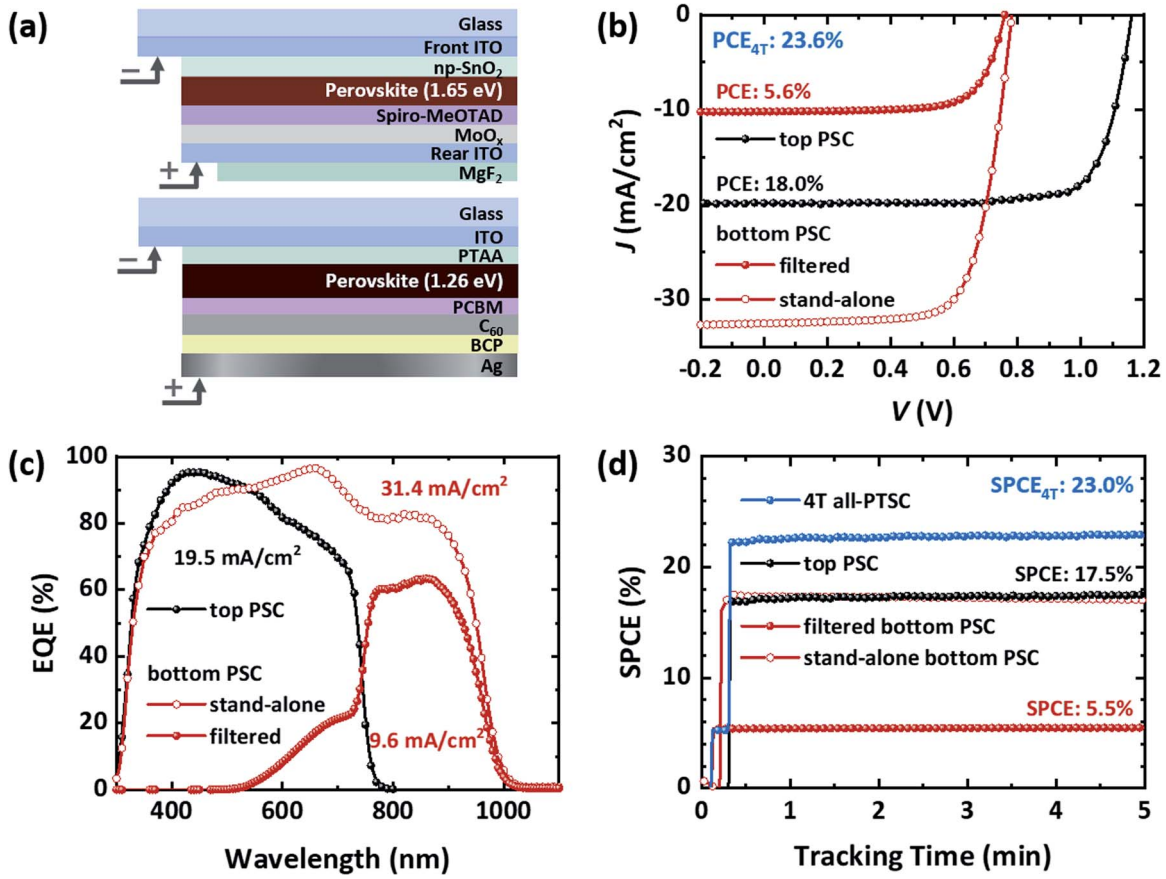

Fig. 5 (a) Schematic cross-sectional image of a 4T all-perovskite tandem solar cell (4T all-PTSC) configuration, implementing a semi-transparent top PSC ($E_g = 1.65$ eV) and a low-bandgap (LBG) bottom PSC (1.26 eV). (b) Current-density–voltage (J–V) scans measured at a fixed rate of 0.6 V s^{-1}, from the open-circuit voltage (V_{OC}) to the short-circuit current (J_{SC}), (c) the external quantum efficiency (EQE), and (d) maximum power point (MPP) tracking measurements, of the semi-transparent top PSC and the LBG bottom PSC (stand-alone and filtered) under AM 1.5G illumination (100 mW cm^{-2}) at 25 °C. PCE_{4T} and $SPCE_{4T}$ are the calculated PCE and stabilized PCE derived from the J–V scans and the MPP tracking measurements for the champion 4T all-PTSC, respectively. The calculated J_{SC} values from the EQE responses for the semi-transparent top, stand-alone LBG bottom, and filtered LBG bottom PSCs are 19.5, 31.4, and 9.6 mA cm^{-2}, respectively.

These observations are also in line with the improved J_{SC} of the PSCs with sufficient Cs concentrations (Fig. S3c†). Finally, another possible explanation for the reduction of the nanosized aggregates could be that the reaction between residual $Sn_yPb_{(1-y)}I_2$ and CsI results in a perovskite with a new composition. To corroborate this hypothesis, we investigate the XRD patterns of $Cs_1Sn_{0.5}Pb_{0.5}I_3$ thin-films, and find that the typical perovskite peaks appear at around 14.5° and 29.1° (Fig. S8†). This attests that incorporating Cs in LBG $FA_{0.8}MA_{0.2}Sn_{0.5}Pb_{0.5}I_3$ with residual $Sn_yPb_{(1-y)}I_2$ in principle might also form a new $Cs_1Sn_{0.5}Pb_{0.5}I_3$ perovskite phase. However, the volume fraction of $Cs_1Sn_{0.5}Pb_{0.5}I_3$, if existed, must be very low, and therefore it would be hard to detect its XRD peaks in the XRD patterns of LBG perovskite thin-films shown in Fig. 4a. In summary, our observations reveal that there is an excess of Sn and Pb in the form of $Sn_yPb_{(1-y)}I_2$ ($0 < y < 1$) on the surface of $FA_{0.8}MA_{0.2}Sn_{0.5}Pb_{0.5}I_3$ LBG perovskite thin-films that diminishes by only adding minute amounts of Cs. Reaction between residual $Sn_yPb_{(1-y)}I_2$ and Cs results in a volumetric growth of the LBG perovskite thin-films and leads to an enhanced crystallinity. This results in remarkably improved photo-stability of the respective PSCs.

Lastly, combining the LBG PSCs with Cs2.5% ($E_g = 1.26$ eV) with semi-transparent PSCs ($E_g = 1.65$ eV), we fabricate 4T all-PTSCs, as schematically illustrated in Fig. 5a. The semi-transparent PSC composed of a 2D/3D perovskite heterostructure has a regular configuration of glass/ITO/SnO_2 nanoparticles (np-SnO_2)/$Cs_{0.17}FA_{0.83}Pb(I_{0.76}Br_{0.24})_3$/2,2′,7,7′-tetrakis [*N*,*N*-di(4-methoxyphenyl)amino]-9,9′-spirobifluorene (spiro-MeOTAD)/molybdenum oxide (MoO_x)/ITO/magnesium fluoride (MgF_2).[8] MoO_x (10 nm) is to protect the spiro-MeOTAD layer against ion bombardment during the subsequent ITO sputtering process.[74,75] In addition, an MgF_2 thin-film (165 nm) on the sputtered ITO acts as an anti-reflection to increase the optical transmittance.[76] The UV-vis absorbance spectra and the Tauc plots of the perovskite absorber layers applied for the semi-transparent top and the LBG bottom PSCs are presented in Fig. S9.† The best performing semi-transparent PSC and LBG PSC with Cs2.5% attain PCEs of 18.0% and 18.2%, respectively. Applying a semi-transparent perovskite filter (substrate area 225 mm^2), which is fabricated under the same conditions and has the same structure as the semi-transparent PSCs, on top of the LBG PSCs, a PCE of 5.6% is attainable. By adding the PCE of the semi-transparent top PSC (=18.0%) and the PCE of the filtered LBG bottom PSC (=5.6%), we determine the efficiency of the corresponding 4T all-PTSC to be 23.6%. Fig. S10a and b† exhibit the transmittance (T), reflectance (R), and absorptance (A) spectra of a semi-transparent filter and an LBG perovskite thin-film with Cs2.5% deposited on PTAA-coated ITO, respectively. In addition, we compare the UV-vis spectra of the semi-transparent filters and semi-transparent PSCs (Fig. S11,† shown only for one filter and one cell) and observe an insignificant difference. The calculated J_{SC} values from the integration of EQE spectra (Fig. 5c) are 19.5, 31.4, and 9.6 mA cm^{-2} for the semi-transparent top, stand-alone LBG bottom, and filtered LBG bottom PSCs, respectively. Table 1 summarizes the photovoltaic parameters for the champion top and bottom PSCs, as well as the calculated PCE of the corresponding 4T all-PTSCs. Similarly, we achieve promising results for the SPCEs (Fig. 5d). The semi-transparent top PSC provides a SPCE of 17.5%, whereas the bottom PSC has a SPCE of 17.5% (stand-alone) and 5.5% (filtered) from the MPP tracking under constant AM 1.5G illumination at 25 °C. Thereby, the corresponding 4T all-PTSC provides a SPCE of 23.0% by adding the SPCE values of the semi-transparent top PSC (=17.5%) and the filtered LBG bottom PSC (=5.5%). Furthermore, using a polydimethylsiloxane (PDMS) anti-reflection foil with a randomly inverted pyramid texture at the front-side of the semi-transparent PSC leads to a boost in the J_{SC} by 1 mA cm^{-2} (compare J–V scans of the semi-transparent top PSC provided in Fig. 5b and S12a†). The PDMS foils are used to reduce the front-surface reflection losses.[77–80] The textured PDMS foil we use here significantly reduces the reflectance from the glass ITO substrates (Fig. S13†). Therefore, by applying the PDMS foil, a single-junction semi-transparent PSC with a PCE and a SPCE as high as 18.9% and 18.3% is achievable (Fig. S12†). Applying the PDMS foil on the semi-transparent filter improves the PCE of the filtered LBG bottom PSC to 6.5%. Thereby, the PCE of the respective 4T all-PTSC is enhanced to 25.4%, if using a PDMS foil while measuring the sub-PSCs (Fig. S12 and Table S2†). Our results demonstrate the potential of the Cs-incorporated LBG perovskite thin-films in configuring high-efficiency 4T all-PTSCs with improved operational photo-stability. Future research should consider the potential improvement in the efficiency

Table 1 Photovoltaic parameters of champion semi-transparent top PSC and low-bandgap (LBG) bottom PSC (stand-alone and filtered), derived from current-density–voltage (J–V) scans measured at a fixed rate of 0.6 V s^{-1} from the open-circuit voltage (V_{OC}) to the short-circuit current (J_{SC}) (backward scan) and from J_{SC} to V_{OC} (forward scan). The stabilized PCE (SPCE) values of the top and filtered bottom perovskite solar cells and the corresponding calculated 4T all-perovskite tandem solar cell (all-PTSC) are given in bold

Perovskite solar cell (PSC)	Scan direction	V_{OC} (V)	J_{SC} (mA cm^{-2})	FF (%)	PCE (%)	SPCE (%)
Semi-transparent top PSC	Backward	1.16	19.7	78.7	**18.0**	**17.5**
	Forward	1.13	20.0	74.8	**16.9**	
LBG bottom PSC (stand-alone)	Backward	0.78	32.5	71.8	18.2	17.5
	Forward	0.77	32.5	66.5	16.7	
LBG bottom PSC (filtered)	Backward	0.76	10.2	72.2	**5.6**	**5.5**
	Forward	0.75	10.2	68.4	**5.2**	
4T all-PTSC	Backward				**23.6**	**23.0**
	Forward				**22.1**	

and the stability of the Cs-incorporated LBG PSCs through established methods such as incorporating antioxidant additives, applying 2D components as passivation layers, and introducing alternative cations into the perovskite lattice structure such as rubidium and potassium.

3. Conclusion

In summary, we demonstrate that incorporating only minute quantities of Cs in double-cation Sn–Pb-based perovskite thin-films effectively improves the operational photo-stability of the low-bandgap PSCs. The $Cs_x(FA_{0.8}MA_{0.2})_{(1-x)}Sn_{0.5}Pb_{0.5}I_3$ low-bandgap PSCs with $x = 2.5\%$ attain remarkable PCE as high as 18.2%. More importantly, perovskite solar cells prepared with $x = 2.5\%$ and 5% respectively maintain 92% and 99% of their initial PCE after 120 min of the MPP tracking under constant AM 1.5G solar illumination. Our observations demonstrate that the introduction of small quantities of Cs considerably reduces the formation of residual nanosized $Sn_yPb_{(1-y)}I_2$ (with $0 < y < 1$) aggregates on the surface of the LBG perovskite thin-films, which is attributed to the reaction of Cs with the residual $Sn_yPb_{(1-y)}I_2$ and results in a volumetric growth of the perovskite thin-films. Furthermore, a beneficial stoichiometric composition and better crystallinity of the perovskite absorber is demonstrated for a sufficient amount of Cs that leads to an improvement in the photo-stability of the respective PSCs. Applying the low-bandgap PSCs together with semi-transparent top PSCs, we attain a 4T all-perovskite tandem solar cell with a PCE of 23.6% and a stabilized PCE of 23.0%, which are among the highest values reported to date in the literature.

4. Experimental section

4.1. Preparation of perovskite precursor solution

For the triple-cation LBG perovskite precursor solution with the stoichiometric formula of $Cs_x(FA_{0.8}MA_{0.2})_{(1-x)}Sn_{0.5}Pb_{0.5}I_3$, we first prepared the double-cation $FA_{0.8}MA_{0.2}Sn_{0.5}Pb_{0.5}I_3$ perovskite precursor solution by dissolving 1.1 M formamidinium iodide (FAI, Dyesol), 0.3 M methylammonium iodide (MAI, Dyesol), 0.7 M tin iodide (SnI_2, Alfa Aesar, 99.999%), 0.7 M lead iodide (PbI_2, Alfa Aesar, 99.999%), 0.008 M lead thiocyanate ($Pb(SCN)_2$, Sigma Aldrich, 99.5%), and 0.045 M tin fluoride (SnF_2, Sigma Aldrich, 99%) in a 9 : 1 (v/v) mixture of dimethylformamide (DMF, Sigma Aldrich, anhydrous, 99.8%) and dimethyl sulfoxide (DMSO, Sigma Aldrich, anhydrous, ≥99.9%). Next, we prepared the cesium iodide (CsI, Alpha Aesar) stock solution by dissolving 1.5 M CsI in DMSO. By adding 8.8, 21.8, 42.4, and 80.4 μl of the 1.5 M CsI stock into 1 ml of the double-cation $FA_{0.8}MA_{0.2}Sn_{0.5}Pb_{0.5}I_3$ perovskite precursor solution, we prepared the final triple-cation $Cs_x(FA_{0.8}MA_{0.2})_{(1-x)}Sn_{0.5}Pb_{0.5}I_3$ perovskite solution for $x = 0.01$, 0.025, 0.05, and 0.1, respectively. After preparation, the solution was stored for 1 hour before fabrication in an N_2-filled glovebox ($O_2 < 0.2$ ppm and $H_2O < 0.4$ ppm). For the $Cs_x(FA_{0.8}MA_{0.2})_{(1-x)}Sn_{0.5}Pb_{0.5}I_3$ perovskite thin-films with Sn and Pb excess, we added additional PbI_2 and SnI_2 to $FA_{0.8}MA_{0.2}Sn_{0.5}Pb_{0.5}I_3$ in order to achieve the required 7.5% excess $Sn_{0.5}Pb_{0.5}I_2$, followed by adding Cs from a 1.5 M stock solution to reach 3%, 7.5%, and 12.5% Cs concentrations. For the double-cation perovskite precursor solution with the stoichiometric formula of $Cs_{0.17}FA_{0.83}Pb(I_{0.76}Br_{0.24})_3$, we mixed 0.83 mmol FAI, 0.17 mmol CsI, 0.64 mmol PbI_2, and 0.36 mmol $PbBr_2$ in a 4 : 1 (v/v) mixture of DMF : DMSO.

4.2. Solar cell fabrication

We fabricated the triple-cation LBG PSCs with an active area of 10.5 mm^2 and a layer sequence of glass/indium tin oxide (ITO)/poly[bis(4-phenyl)(2,4,6-trimethylphenyl)amine] (PTAA)/$Cs_x(FA_{0.8}MA_{0.2})_{(1-x)}Sn_{0.5}Pb_{0.5}I_3$/phenyl-$C_{61}$-butyric acid methyl ester (PCBM)/buckminsterfullerene (C_{60})/2,9-dimethyl-4,7-diphenyl-1,10-phenanthroline (BCP)/silver (Ag). Initially, we cleaned the 16 × 16 mm^2 glass substrates coated with 120 nm thick ITO layers (sheet resistance 15 Ω sq^{-1}, Luminescence Technology) in an ultrasonic bath with acetone and isopropanol for 10 min each followed by an oxygen plasma treatment at 100 W power for 3 min. We spin-coated the glass ITO substrates with a ∼5 nm thin-film of PTAA (M_w = 17 800 g mol^{-1}, EM INDEX), as the hole transport layer at 4000 rpm for 30 s, followed by annealing at 100 °C for 30 min. Next, we deposited the LBG perovskite thin-film on the PTAA-coated substrates at 5000 rpm for 10 s. We immediately vacuum-exposed the layers for 10 s in a vacuum chamber (∼10 Pa) with a 150 ml volume size. We, sequentially, annealed the perovskite thin-films at 100 °C for 7 min. Next, we spin-coated the perovskite thin-film by a ∼5 nm thin-film of PCBM (Sigma Aldrich, 99.5%), which was prepared by dissolving 5 mg PCBM in 1 ml 1,2-dichlorobenzene (Sigma Aldrich, anhydrous, 99%) and spin-coated at 4000 rpm for 60 s. In sequence, we used a Lesker PVD system to thermally evaporate ∼20 nm of C_{60} (Sigma Aldrich, 99.5%) and ∼5 nm of BCP (Luminescence Technology) as the electron transport material, in 6 × 10^{-6} mbar pressure and at a rate of 0.1–0.2 and 0.2–0.3 Å s^{-1}, respectively. We completed the PSC stack by evaporating a back contact of Ag (∼100 nm).

To fabricate the transparent double-cation PSCs with the same active area (10.5 mm^2) and a layer sequence of ITO/SnO_2 nanoparticles/$Cs_{0.17}FA_{0.83}Pb(I_{0.76}Br_{0.24})_3$/2,2′,7,7′-tetrakis[*N*,*N*-di(4-methoxyphenyl)amino]-9,9′-spirobifluorene (spiro-MeOTAD)/molybdenum oxide (MoO_x)/ITO/magnesium fluoride (MgF_2), we used sputtered ITO thin-films applying a Kurt J Lesker PVD-75 thin-film deposition system. The following sputtering parameters were used for the front (rear) ITO: power = 50 W (50 W), substrate temperature = 300 °C (25 °C), deposition time = 2000 s (2300 s), pressure = 0.8 mTorr (0.8 mTorr), O_2 partial pressure = 3.5% (2.5%), and thickness ∼135 nm (150 nm). The sheet resistance of the sputtered ITO was 10–12 Ω sq^{-1} (40–50 Ω sq^{-1}). First, we spin-coated the pre-cleaned ITO substrates with SnO_2 nanoparticles (Alfa Aesar, diluted in distilled water to a concentration of 2.04%) at 4000 rpm for 30 s, followed by a 250 °C annealing step for 30 min in an ambient atmosphere. Next, we deposited the double-cation perovskite absorber layer from solution by a two-step spin coating process: (i) 1000 rpm for 10 s, (ii) 5000 rpm for 30 s, while10 s before the end of the second step 100 μl chlorobenzene was poured on the spinning substrate. Annealing the samples at 100 °C for 30 min in an inert atmosphere was next. After the annealing step, we processed the

2D/3D perovskite heterostructure by spin-coating 100 μl *n*-butylammonium bromide (BABr, Dysol) dissolved in isopropanol (2 mg ml^{-1}) at 5000 rpm for 30 s on top of the perovskite thin-film with subsequent annealing at 100 °C for 5 min in an inert atmosphere. Next, we deposited spiro-MeOTAD as the hole transport layer using a spin-coating process with 4000 rpm for 30 s. A 10 nm thin-film of MoO_x (Sigma Aldrich) was thermally evaporated on spiro-MeOTAD using a Lesker PVD system at a rate of 0.8 Å s^{-1} and in 6×10^{-6} mbar pressure. To increase the conductivity of the rear ITO, we thermal-evaporated ~75 nm Au fingers at a rate of 2 Å s^{-1} using a shadow mask. We completed the stack by depositing ~165 nm MgF_2 as an anti-reflection layer on top of the rear ITO using a Lesker PVD system at a rate of 3–4 Å s^{-1} and in 6×10^{-6} mbar pressure.

4.3. Characterization

Current-density–voltage (*J–V*) measurements. We used xenon-lamp solar simulator (Newport Oriel Sol3A) providing an air-mass 1.5 global (AM1.5G) spectra (100 mW cm^{-2}) to measure the *J–V* characteristics of the PSCs with a scan rate set at 0.6 V s^{-1} using a sourcemeter (Keithley 2400). We calibrated the irradiation intensity using a certified silicon reference solar cell (KG5, Newport). We determined the stable power conversion efficiency of the PSCs by measuring the photocurrent at the maximum power point (MPP) over 5 and 120 min, while the temperature of the devices was set at 25 °C using a Peltier element connected to a microcontroller while performing the *J–V* analyses and MPP measurements.

External quantum efficiency measurements (EQE). Using a Bentham EQE system, we performed the EQE measurements, applying a chopping frequency of ~930 Hz with an integration time of 500 ms to obtain the spectra. The devices were not subjected to any preconditioning. We used a large illumination spot to average over possible variations in the EQE spectra of the LBG bottom PSC while using the top perovskite filter. The possible variations could be induced by inhomogeneous scattering and transmission properties due to typical thickness variations of the double-cation $Cs_{0.17}FA_{0.83}Pb(I_{0.76}Br_{0.24})_3$ perovskite filter.

Scanning electron microscopy (SEM). We obtained high-resolution field cross-sectional and top-view field emission SEM images of the LBG perovskite thin-films using a Zeiss Supra60 VP scanning electron microscope. The SEM images were captured using a 3 kV acceleration voltage.

X-ray diffraction (XRD). We utilized a Bruker D2Phaser system with Cu-K_α radiation (λ = 1.5405 Å) to determine the crystalline structure of perovskite thin-films. Perovskite layers were covered with a layer of poly(methyl methacrylate) (PMMA) to be protected from oxidation. An N_2-filled sealed holder was used to keep the samples in the inert condition while characterizing PbI_2, SnI_2, and $Sn_{0.5}Pb_{0.5}I_2$ thin-films.

Cathodoluminescence (CL). We performed the CL measurement on the FEI Verios scanning electron microscope (SEM) equipped with a Gatan MonoCL4 Elite cathodoluminescence system. It should be noted that although CL is a powerful technique to study the electronic properties of perovskite materials, irradiation conditions should be meticulously controlled to avoid any significant beam damage. The CL spectrum was obtained at a constant accelerating voltage of 5 kV with a beam current of 22 pA.

UV-vis spectrophotometry. We used a Bentham PVE300 photovoltaic service characterization system (located in an N_2-filled glovebox) to measure the transmittance and reflectance spectra of the perovskite thin-films.

X-ray photoelectron spectroscopy (XPS). The base pressure of the XPS analysis chamber is ~7×10^{-11} mbar. The XPS measurements were performed with an Omicron Argus CU electron analyzer and a non-monochromatized DAR 450 twin anode X-ray source providing Mg-K_α and Al-K_α X-rays. The energy axis was calibrated using a sputter-cleaned Au, Ag, and Cu foil.[81] For all measurements, no charging was observed. The emission angle of the electrons is perpendicular to the surface. This leads to a characteristic attenuation length (λ) of 1–3 nm. To prevent an influence of beam-induced changes from the X-rays on the spectra, the measurement times were kept <10 min. This upper limit of the measurement time was determined in time-resolved measurements.

Surface profile and thickness. The thickness of the perovskite layers was measured using a Bruker Dektakt XT profilometer.

Conflicts of interest

There are no conflicts to declare.

Acknowledgements

We acknowledge support by the KIT-Publication Fund of the Karlsruhe Institute of Technology. We would like to thank Dirk Hauschild (KIT) and Lothar Weinhardt (KIT) for XPS measurements. S. M. would like to acknowledge the financial support from DAAD (Deutscher Akademischer Austauschdienst/German academic exchange service) for her doctoral research work under personal reference number 91621525. The financial support by Alexander von Humboldt (Georg Forster Research Fellowship), German Federal Ministry of Education and Research (BMBF) through PRINTPERO (03SF0557A) project, German Federal Ministry for Economic Affairs and Energy (CAPITANO, funding code: 03EE1038B), the Initiating and Networking funding of Helmholtz Association HYIG of U.W.P. (VH-NG-1148), Helmholtz Energy Materials Foundry (HEMF), PEROSEED (ZT-0024), Science and Technology of Nanostructures (STN), and Karlsruhe School of Optics & Photonics (KSOP) is gratefully acknowledged. T. D. acknowledges the financial support of a Postdoc Fellowship from the Australian Centre for Advanced Photovoltaics (ACAP). Part of the experiment was performed at the Australian National Fabrication Facility (ANFF) ACT Node.

References

1 A. Kojima, K. Teshima, Y. Shirai and T. Miyasaka, *J. Am. Chem. Soc.*, 2009, **131**, 6050–6051.

2 https://www.nrel.gov/pv/assets/pdfs/best-research-cell-efficiencies.20200128.pdf, accessed 25 September 2020.
3 W. Shockley and H. J. Queisser, *J. Appl. Phys.*, 1961, **32**, 510–519.
4 F. Hao, C. C. Stoumpos, R. P. H. Chang and M. G. Kanatzidis, *J. Am. Chem. Soc.*, 2014, **136**, 8094–8099.
5 J. Im, C. C. Stoumpos, H. Jin, A. J. Freeman and M. G. Kanatzidis, *J. Phys. Chem. Lett.*, 2015, **6**, 3503–3509.
6 J. H. Noh, S. H. Im, J. H. Heo, T. N. Mandal and S. Il Seok, *Nano Lett.*, 2013, **13**, 1764–1769.
7 X. Zhang, J. Liu, Z. Song, W. Zuo, Z. Fan, X. He, K. Luo, Q. Ye and C. Liao, *Phys. Status Solidi*, 2019, **216**, 1800727.
8 S. Gharibzadeh, I. M. Hossain, P. Fassl, B. A. Nejand, T. Abzieher, M. Schultes, E. Ahlswede, P. Jackson, M. Powalla, S. Schäfer, M. Rienäcker, T. Wietler, R. Peibst, U. Lemmer, B. S. Richards and U. W. Paetzold, *Adv. Funct. Mater.*, 2020, **30**, 1909919.
9 D. P. McMeekin, G. Sadoughi, W. Rehman, G. E. Eperon, M. Saliba, M. T. Horantner, A. Haghighirad, N. Sakai, L. Korte, B. Rech, M. B. Johnston, L. M. Herz and H. J. Snaith, *Science*, 2016, **351**, 151–155.
10 S. Gharibzadeh, B. Abdollahi Nejand, M. Jakoby, T. Abzieher, D. Hauschild, S. Moghadamzadeh, J. A. Schwenzer, P. Brenner, R. Schmager, A. A. Haghighirad, L. Weinhardt, U. Lemmer, B. S. Richards, I. A. Howard and U. W. Paetzold, *Adv. Energy Mater.*, 2019, **9**, 1803699.
11 D. Zhao, C. Wang, Z. Song, Y. Yu, C. Chen, X. Zhao, K. Zhu and Y. Yan, *ACS Energy Lett*, 2018, **3**, 305–306.
12 D. Zhao, Y. Yu, C. Wang, W. Liao, N. Shrestha, C. R. Grice, A. J. Cimaroli, L. Guan, R. J. Ellingson, K. Zhu, X. Zhao, R.-G. Xiong and Y. Yan, *Nat. Energy*, 2017, **2**, 17018.
13 G. E. Eperon, T. Leijtens, K. A. Bush, R. Prasanna, T. Green, J. T. W. Wang, D. P. McMeekin, G. Volonakis, R. L. Milot, R. May, A. Palmstrom, D. J. Slotcavage, R. A. Belisle, J. B. Patel, E. S. Parrott, R. J. Sutton, W. Ma, F. Moghadam, B. Conings, A. Babayigit, H. G. Boyen, S. Bent, F. Giustino, L. M. Herz, M. B. Johnston, M. D. McGehee and H. J. Snaith, *Science*, 2016, **354**, 861–865.
14 T. Leijtens, R. Prasanna, K. A. Bush, G. E. Eperon, J. A. Raiford, A. Gold-Parker, E. J. Wolf, S. A. Swifter, C. C. Boyd, H.-P. Wang, M. F. Toney, S. F. Bent and M. D. McGehee, *Sustain. Energy Fuels*, 2018, **2**, 2450–2459.
15 M. Anaya, J. P. Correa-Baena, G. Lozano, M. Saliba, P. Anguita, B. Roose, A. Abate, U. Steiner, M. Grätzel, M. E. Calvo, A. Hagfeldt and H. Míguez, *J. Mater. Chem. A*, 2016, **4**, 11214–11221.
16 B. Abdollahi Nejand, I. M. Hossain, M. Jakoby, S. Moghadamzadeh, T. Abzieher, S. Gharibzadeh, J. A. Schwenzer, P. Nazari, F. Schackmar, D. Hauschild, L. Weinhardt, U. Lemmer, B. S. Richards, I. A. Howard and U. W. Paetzold, *Adv. Energy Mater.*, 2020, **10**, 1902583.
17 J. Tong, Z. Song, D. H. Kim, X. Chen, C. Chen, A. F. Palmstrom, P. F. Ndione, M. O. Reese, S. P. Dunfield, O. G. Reid, J. Liu, F. Zhang, S. P. Harvey, Z. Li, S. T. Christensen, G. Teeter, D. Zhao, M. M. Al-Jassim, M. F. A. M. van Hest, M. C. Beard, S. E. Shaheen, J. J. Berry, Y. Yan and K. Zhu, *Science*, 2019, **364**, 475–479.
18 R. Lin, K. Xiao, Z. Qin, Q. Han, C. Zhang, M. Wei, M. I. Saidaminov, Y. Gao, J. Xu, M. Xiao, A. Li, J. Zhu, E. H. Sargent and H. Tan, *Nat. Energy*, 2019, **4**, 864–873.
19 S. Ternes, T. Börnhorst, J. A. Schwenzer, I. M. Hossain, T. Abzieher, W. Mehlmann, U. Lemmer, P. Scharfer, W. Schabel, B. S. Richards and U. W. Paetzold, *Adv. Energy Mater.*, 2019, **9**, 1901581.
20 T. Abzieher, J. A. Schwenzer, S. Moghadamzadeh, F. Sutterluti, I. M. Hossain, M. Pfau, E. Lotter, M. Hetterich, B. S. Richards, U. Lemmer, M. Powalla and U. W. Paetzold, *IEEE J. Photovoltaics*, 2019, **9**, 1249–1257.
21 T. Abzieher, S. Moghadamzadeh, F. Schackmar, H. Eggers, F. Sutterlüti, A. Farooq, D. Kojda, K. Habicht, R. Schmager, A. Mertens, R. Azmi, L. Klohr, J. A. Schwenzer, M. Hetterich, U. Lemmer, B. S. Richards, M. Powalla and U. W. Paetzold, *Adv. Energy Mater.*, 2019, **9**, 1802995.
22 B. Zhao, M. Abdi-Jalebi, M. Tabachnyk, H. Glass, V. S. Kamboj, W. Nie, A. J. Pearson, Y. Puttisong, K. C. Gödel, H. E. Beere, D. A. Ritchie, A. D. Mohite, S. E. Dutton, R. H. Friend and A. Sadhanala, *Adv. Mater.*, 2017, **29**, 1604744.
23 W. Liao, D. Zhao, Y. Yu, N. Shrestha, K. Ghimire, C. R. Grice, C. Wang, Y. Xiao, A. J. Cimaroli, R. J. Ellingson, N. J. Podraza, K. Zhu, R.-G. Xiong and Y. Yan, *J. Am. Chem. Soc.*, 2016, **138**, 12360–12363.
24 E. S. Parrott, T. Green, R. L. Milot, M. B. Johnston, H. J. Snaith and L. M. Herz, *Adv. Funct. Mater.*, 2018, **28**, 1802803.
25 T. Leijtens, R. Prasanna, A. Gold-Parker, M. F. Toney and M. D. McGehee, *ACS Energy Lett*, 2017, **2**, 2159–2165.
26 Z. Shi, J. Guo, Y. Chen, Q. Li, Y. Pan, H. Zhang, Y. Xia and W. Huang, *Adv. Mater.*, 2017, **29**, 1605005.
27 K. P. Marshall, M. Walker, R. I. Walton and R. A. Hatton, *Nat. Energy*, 2016, **1**, 16178.
28 M. H. Kumar, S. Dharani, W. L. Leong, P. P. Boix, R. R. Prabhakar, T. Baikie, C. Shi, H. Ding, R. Ramesh, M. Asta, M. Graetzel, S. G. Mhaisalkar and N. Mathews, *Adv. Mater.*, 2014, **26**, 7122–7127.
29 T. M. Koh, T. Krishnamoorthy, N. Yantara, C. Shi, W. L. Leong, P. P. Boix, A. C. Grimsdale, S. G. Mhaisalkar and N. Mathews, *J. Mater. Chem. A*, 2015, **3**, 14996–15000.
30 S. Gupta, D. Cahen and G. Hodes, *J. Phys. Chem. C*, 2018, **122**, 13926–13936.
31 M. C. Jung, S. R. Raga and Y. Qi, *RSC Adv.*, 2016, **6**, 2819–2825.
32 C.-M. Tsai, H.-P. Wu, S.-T. Chang, C.-F. Huang, C.-H. Wang, S. Narra, Y.-W. Yang, C.-L. Wang, C.-H. Hung and E. W.-G. Diau, *ACS Energy Lett*, 2016, **1**, 1086–1093.
33 X. Xu, C.-C. Chueh, Z. Yang, A. Rajagopal, J. Xu, S. B. Jo and A. K. Y. Jen, *Nano Energy*, 2017, **34**, 392–398.
34 Q. Tai, X. Guo, G. Tang, P. You, T. W. Ng, D. Shen, J. Cao, C. K. Liu, N. Wang, Y. Zhu, C. S. Lee and F. Yan, *Angew. Chemie - Int. Ed.*, 2019, **58**, 806–810.
35 M. Wei, K. Xiao, G. Walters, R. Lin, Y. Zhao, M. I. Saidaminov, P. Todorović, A. Johnston, Z. Huang, H. Chen, A. Li, J. Zhu, Z. Yang, Y. Wang, A. H. Proppe,

S. O. Kelley, Y. Hou, O. Voznyy, H. Tan and E. H. Sargent, *Adv. Mater.*, 2020, **32**, 1907058.
36 Z. Chen, M. Liu, Z. Li, T. Shi, Y. Yang, H.-L. Yip and Y. Cao, *iScience*, 2018, **9**, 337–346.
37 E. Ruggeri, M. Anaya, K. Gałkowski, G. Delport, F. U. Kosasih, A. Abfalterer, S. Mackowski, C. Ducati and S. D. Stranks, *Adv. Mater.*, 2019, **31**, 1905247.
38 X. Liu, Z. Yang, C.-C. Chueh, A. Rajagopal, S. T. Williams, Y. Sun and A. K. Y. Jen, *J. Mater. Chem. A*, 2016, **4**, 17939–17945.
39 T. Jiang, Z. Chen, X. Chen, T. Liu, X. Chen, W. E. I. Sha, H. Zhu and Y. Yang, *Sol. RRL*, 2020, **4**, 1900467.
40 E. J. Juarez-Perez, L. K. Ono and Y. Qi, *J. Mater. Chem. A*, 2019, **7**, 16912–16919.
41 E. J. Juarez-Perez, L. K. Ono, M. Maeda, Y. Jiang, Z. Hawash and Y. Qi, *J. Mater. Chem. A*, 2018, **6**, 9604–9612.
42 W. Nie, J.-C. Blancon, A. J. Neukirch, K. Appavoo, H. Tsai, M. Chhowalla, M. A. Alam, M. Y. Sfeir, C. Katan, J. Even, S. Tretiak, J. J. Crochet, G. Gupta and A. D. Mohite, *Nat. Commun.*, 2016, **7**, 11574.
43 F. Arabpour Roghabadi, M. Alidaei, S. M. Mousavi, T. Ashjari, A. S. Tehrani, V. Ahmadi and S. M. Sadrameli, *J. Mater. Chem. A*, 2019, **7**, 5898–5933.
44 C. C. Stoumpos, C. D. Malliakas and M. G. Kanatzidis, *Inorg. Chem.*, 2013, **52**, 9019–9038.
45 Z. Li, M. Yang, J.-S. Park, S.-H. Wei, J. J. Berry and K. Zhu, *Chem. Mater.*, 2016, **28**, 284–292.
46 M. Saliba, T. Matsui, J.-Y. Seo, K. Domanski, J.-P. Correa-Baena, M. K. Nazeeruddin, S. M. Zakeeruddin, W. Tress, A. Abate, A. Hagfeldt and M. Grätzel, *Energy Environ. Sci.*, 2016, **9**, 1989–1997.
47 Y. Hu, E. M. Hutter, P. Rieder, I. Grill, J. Hanisch, M. F. Aygüler, A. G. Hufnagel, M. Handloser, T. Bein, A. Hartschuh, K. Tvingstedt, V. Dyakonov, A. Baumann, T. J. Savenije, M. L. Petrus and P. Docampo, *Adv. Energy Mater.*, 2018, **8**, 1703057.
48 G. Kapil, T. Bessho, C. H. Ng, K. Hamada, M. Pandey, M. A. Kamarudin, D. Hirotani, T. Kinoshita, T. Minemoto, Q. Shen, T. Toyoda, T. N. Murakami, H. Segawa and S. Hayase, *ACS Energy Lett*, 2019, **4**, 1991–1998.
49 C. Li, Z. Song, D. Zhao, C. Xiao, B. Subedi, N. Shrestha, M. M. Junda, C. Wang, C. S. Jiang, M. Al-Jassim, R. J. Ellingson, N. J. Podraza, K. Zhu and Y. Yan, *Adv. Energy Mater.*, 2019, **9**, 1803135.
50 D. Zhao, C. Chen, C. Wang, M. M. Junda, Z. Song, C. R. Grice, Y. Yu, C. Li, B. Subedi, N. J. Podraza, X. Zhao, G. Fang, R. G. Xiong, K. Zhu and Y. Yan, *Nat. Energy*, 2018, **3**, 1093–1100.
51 B. Roose, A. Ummadisingu, J.-P. Correa-Baena, M. Saliba, A. Hagfeldt, M. Graetzel, U. Steiner and A. Abate, *Nano Energy*, 2017, **39**, 24–29.
52 N. Ito, M. A. Kamarudin, D. Hirotani, Y. Zhang, Q. Shen, Y. Ogomi, S. Iikubo, T. Minemoto, K. Yoshino and S. Hayase, *J. Phys. Chem. Lett.*, 2018, **9**, 1682–1688.
53 C. Fei and H. Wang, *Org. Electron.*, 2019, **68**, 143–150.
54 T. T. Ngo, E. M. Barea, R. Tena-Zaera and I. Mora-Seró, *ACS Appl. Energy Mater.*, 2018, **1**, 4057–4064.
55 S. Moghadamzadeh, I. M. Hossain, M. Jakoby, B. Abdollahi Nejand, D. Rueda-Delgado, J. A. Schwenzer, S. Gharibzadeh, T. Abzieher, M. R. Khan, A. A. Haghighirad, I. A. Howard, B. S. Richards, U. Lemmer and U. W. Paetzold, *J. Mater. Chem. A*, 2020, **8**, 670–682.
56 H. Do Kim, H. Ohkita, H. Benten and S. Ito, *Adv. Mater.*, 2016, **28**, 917–922.
57 A. F. Castro-Méndez, J. Hidalgo and J. P. Correa-Baena, *Adv. Energy Mater.*, 2019, **9**, 1–10.
58 W. Chen, Y. Wang, G. Pang, C. W. Koh, A. B. Djurišić, Y. Wu, B. Tu, F. Liu, R. Chen, H. Y. Woo, X. Guo and Z. He, *Adv. Funct. Mater.*, 2019, **29**, 1808855.
59 M. M. Tavakoli, M. Saliba, P. Yadav, P. Holzhey, A. Hagfeldt, S. M. Zakeeruddin and M. Grätzel, *Adv. Energy Mater.*, 2019, **9**, 1802646.
60 J. Schoonman, *Chem. Phys. Lett.*, 2015, **619**, 193–195.
61 F. Liu, Q. Dong, M. K. Wong, A. B. Djurišić, A. Ng, Z. Ren, Q. Shen, C. Surya, W. K. Chan, J. Wang, A. M. C. Ng, C. Liao, H. Li, K. Shih, C. Wei, H. Su and J. Dai, *Adv. Energy Mater.*, 2016, **6**, 1502206.
62 Y. H. Lee, J. Luo, R. Humphry-Baker, P. Gao, M. Grätzel and M. K. Nazeeruddin, *Adv. Funct. Mater.*, 2015, **25**, 3925–3933.
63 T. J. Jacobsson, J.-P. Correa-Baena, E. Halvani Anaraki, B. Philippe, S. D. Stranks, M. E. F. Bouduban, W. Tress, K. Schenk, J. Teuscher, J.-E. Moser, H. Rensmo and A. Hagfeldt, *J. Am. Chem. Soc.*, 2016, **138**, 10331–10343.
64 P. Fassl, V. Lami, A. Bausch, Z. Wang, M. T. Klug, H. J. Snaith and Y. Vaynzof, *Energy Environ. Sci.*, 2018, **11**, 3380–3391.
65 B. Roose, K. Dey, Y.-H. Chiang, R. H. Friend and S. D. Stranks, *J. Phys. Chem. Lett.*, 2020, **11**, 6505–6512.
66 T. Duong, H. Pham, T. C. Kho, P. Phang, K. C. Fong, D. Yan, Y. Yin, J. Peng, M. A. Mahmud, S. Gharibzadeh, B. A. Nejand, I. M. Hossain, M. R. Khan, N. Mozaffari, Y. Wu, H. Shen, J. Zheng, H. Mai, W. Liang, C. Samundsett, M. Stocks, K. McIntosh, G. G. Andersson, U. Lemmer, B. S. Richards, U. W. Paetzold, A. Ho-Ballie, Y. Liu, D. Macdonald, A. Blakers, J. Wong-Leung, T. White, K. Weber and K. Catchpole, *Adv. Energy Mater.*, 2020, **10**, 1903553.
67 C. Xiao, Z. Li, H. Guthrey, J. Moseley, Y. Yang, S. Wozny, H. Moutinho, B. To, J. J. Berry, B. Gorman, Y. Yan, K. Zhu and M. Al-Jassim, *J. Phys. Chem. C*, 2015, **119**, 26904–26911.
68 T. Duong, H. K. Mulmudi, Y. Wu, X. Fu, H. Shen, J. Peng, N. Wu, H. T. Nguyen, D. Macdonald, M. Lockrey, T. P. White, K. Weber and K. Catchpole, *ACS Appl. Mater. Interfaces*, 2017, **9**, 26859–26866.
69 T. Duong, H. K. Mulmudi, H. Shen, Y. L. Wu, C. Barugkin, Y. O. Mayon, H. T. Nguyen, D. Macdonald, J. Peng, M. Lockrey, W. Li, Y. B. Cheng, T. P. White, K. Weber and K. Catchpole, *Nano Energy*, 2016, **30**, 330–340.
70 X. Gao and M. S. Daw, *Phys. Rev. B*, 2008, **77**, 033103.
71 J. O. Dimmock, I. Melngailis and A. J. Strauss, *Phys. Rev. Lett.*, 1966, **16**, 1193–1196.
72 R. G. Niemann, L. Gouda, J. Hu, S. Tirosh, R. Gottesman, P. J. Cameron and A. Zaban, *J. Mater. Chem. A*, 2016, **4**, 17819–17827.
73 F. Brivio, C. Caetano and A. Walsh, *J. Phys. Chem. Lett.*, 2016, **7**, 1083–1087.

74 D. Zhao, C. Zhang, H. Kim and L. J. Guo, *Adv. Energy Mater.*, 2015, **5**, 1500768.
75 K. A. Bush, A. F. Palmstrom, Z. J. Yu, M. Boccard, R. Cheacharoen, J. P. Mailoa, D. P. McMeekin, R. L. Z. Hoye, C. D. Bailie, T. Leijtens, I. M. Peters, M. C. Minichetti, N. Rolston, R. Prasanna, S. Sofia, D. Harwood, W. Ma, F. Moghadam, H. J. Snaith, T. Buonassisi, Z. C. Holman, S. F. Bent and M. D. McGehee, *Nat. Energy*, 2017, **2**, 17009.
76 Q. Han, Y.-T. Hsieh, L. Meng, J.-L. Wu, P. Sun, E.-P. Yao, S.-Y. Chang, S.-H. Bae, T. Kato, V. Bermudez and Y. Yang, *Science*, 2018, **361**, 904–908.
77 S. Manzoor, Z. J. Yu, A. Ali, W. Ali, K. A. Bush, A. F. Palmstrom, S. F. Bent, M. D. McGehee and Z. C. Holman, *Sol. Energy Mater. Sol. Cells*, 2017, **173**, 59–65.
78 S. Dottermusch, R. Schmager, E. Klampaftis, S. Paetel, O. Kiowski, K. Ding, B. S. Richards and U. W. Paetzold, *Prog. Photovoltaics Res. Appl.*, 2019, **27**, 3133.
79 R. Schmager, B. Fritz, R. Hünig, K. Ding, U. Lemmer, B. S. Richards, G. Gomard and U. W. Paetzold, *ACS Photonics*, 2017, **4**, 2687–2692.
80 M. Langenhorst, D. Ritzer, F. Kotz, P. Risch, S. Dottermusch, A. Roslizar, R. Schmager, B. S. Richards, B. E. Rapp and U. W. Paetzold, *ACS Appl. Mater. Interfaces*, 2019, **11**, 35015–35022.
81 C. D. Wagner and G. E. Muilenberg, *Handbook of X-ray photoelectron spectroscopy*, Perkin-Elmer, 1979.